

國立臺灣大學理學院物理學研究所

碩士論文

Department of Physics

College of Science

National Taiwan University

Master Thesis



基於斷帶能隙 n - n 異質結構之三硫族化合物的負差分電阻

Negative Differential Resistance in Trichalcogenide

Based Broken-Gap n - n Heterostructures

李念修

Nian-Xiu Li

指導教授：陳永芳 博士

Advisor: Yang-Fang Chen, Ph.D.

中華民國 112 年 7 月

July 2023

國立臺灣大學碩士學位論文

口試委員會審定書

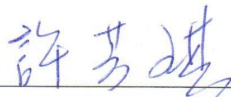
基於斷帶能隙 n-n 異質結構之三硫族化合物的負差分電阻

Negative Differential Resistance in Trichalcogenide Based
Broken-Gap n-n Heterostructures


本論文係李念修君(R10222070)在國立臺灣大學物理學系、所完成之碩士學位論文，於民國 112 年 7 月 21 日承下列考試委員審查通過及口試及格，特此證明

口試委員 Oral examination committee:


(指導教授 Advisor)





系主任/所長 Director: 

誌謝



在我完成這篇論文的過程中，我深感無比的幸運和榮幸，有機會在這個充滿學術探索的旅程中，得到無數人的鼎力支持與幫助。在此，我要衷心向所有在我學術生涯中給予指導、鼓勵和幫助的人表示衷心的感谢。

首先，我要感謝我的導師，陳永芳老師，是您在我學習和研究的過程中給予了無私的指導和支持，使我能夠不斷克服困難，不斷精進。您的學術造詣和對研究的熱情深深影響著我，是您的指導讓我得以在迷失研究方向時找到前進的方向。


我也要感謝 Christy 學姊和夏玉學姊，您們在我研究的過程中提供了寶貴的建議和經驗分享。您們的耐心解答和熱心幫助，使我能夠更深入地理解研究主題，克服了許多困難。您們的示範和鼓勵對我影響深遠，是您們讓我擁有了更豐富的學習經驗。

同時，我要特別感謝其他學長姊們：佑銘、育傑、Rapti、承甫、家宇、育銓、Mujahid 和冠璋；以及同屆的朋友們：政勳、昕恩、道峰、嘉尉和郁軒，是您們在學術和生活上的指導和支持，讓我能夠茁壯成長，不斷追求卓越。您們的榜樣鼓舞著我，讓我知道學習和努力的重要性，並且在我遇到挫折時給予我信心。也謝謝即將升上碩二的學弟妹們，祝福你們能夠順利畢業。

最後，我要感謝我的家人，是您們無條件的支持和鼓勵，讓我能夠專注於學業和研究，追求自己的夢想。您們的愛是我堅強的後盾，是我不斷前行的動力。

雖然文字有限，但我心中的感激之情無法言喻。在這篇論文的每一個字裡，都蘊含著我對您們的感謝之情。無論是誰，您們的支持和幫助對我來說都是至關重要的，謝謝您們。

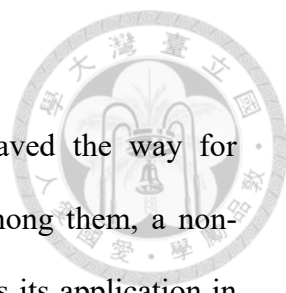
中文摘要



二維半導體異質結構在光電子學領域中為眾多令人興奮的現象鋪平了道路。其中，具有多個閾值的非線性電流-電壓特性在多值邏輯中找到了應用，可以增加電子器件的密度。這種載流子傳輸行為被稱為負差分電阻 (NDR)，其在能帶對能帶隧道效應的幫助下在能帶間斷的能帶對齊異質結構中實現。在這裡，我們展示了在室溫下第 III 型 $\text{ZrS}_3/\text{SnS}_2$ 異質結構中的這種能帶間隧道效應。在室溫下測量的電流-電壓特性曲線中觀察到了明顯的 NDR 效應，其峰谷比 (PVR) 為 1.7。通過製備具有不同幾何形狀和厚度的 ZrS_3 器件，我們仔細研究了電極和 2D 材料之間界面處金屬誘導的能帶狀態對室溫下實現 NDR 效應的影響。結果表明，為了觀察到 NDR 效應，選擇適當的金屬電極非常重要。在雷射照射下，NDR 效應更加顯著，並且在較低的閘極電位下觀察到。由於兩種材料中存在相當小的光學能隙， $\text{ZrS}_3/\text{SnS}_2$ 異質結構可作為光探測器。該器件的光響應度被估計為 300 mA W^{-1} ，用於非常低功率的激光，並且檢測性能的數量級為 10^{10} Jones。因此，所提出的 $\text{ZrS}_3/\text{SnS}_2$ 異質結構展示出顯著的 NDR 效應和合理的光響應度，在近期的奈米電子學領域具有廣泛的應用前景。

關鍵詞：n-n 異質結構、三硫族化合物、負差分電阻、光探測器、費米能階釘扎。

Abstract



Two-dimensional (2D) semiconductor heterojunction has paved the way for numerous exciting phenomena in the field of optoelectronics. Among them, a non-linear current-voltage behavior with multiple threshold values finds its application in multi-valued logic, which can increase the device density in electronics. This carrier transport behavior termed negative differential resistance (NDR) is aided by band-to-band tunneling in the broken-gap energy band-aligned heterostructures. Here, we demonstrate this interband tunneling effect in type-III $\text{ZrS}_3/\text{SnS}_2$ heterostructure at room temperature. A prominent NDR effect with a peak-to-valley ratio (PVR) of 1.7 was observed in the current-voltage characteristic curves measured at room temperature. The effect of the metal-induced gap states at the interface between electrode and 2D material in the realization of the NDR effect at room temperature has been meticulously studied by fabricating ZrS_3 devices with different geometry and thickness. The results indicate that in order to observe NDR effect, the choice of a suitable metal electrode is very important. Under the illumination of a laser, the effect of NDR becomes more pronounced and observed at lower gate potential. The $\text{ZrS}_3/\text{SnS}_2$ heterostructure works as a photodetector due to a considerable optical band gap in both materials. The photoresponsivity of the device was estimated to be 300 mA W^{-1} for a very low laser power and the detectivity was determined to be in the order of 10^{10} Jones. Hence, the proposed $\text{ZrS}_3/\text{SnS}_2$ heterostructure exhibiting a significant NDR effect and reasonable photoresponsivity has a wide scope in the field of nanoelectronics in the near future.

Keywords: *n-n* heterostructure, trichalcogenides, negative differential resistance, photodetector, Fermi level pinning

Contents



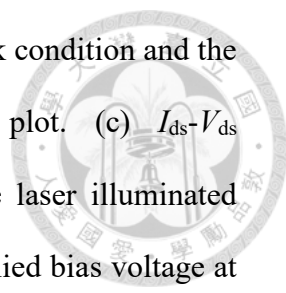
口試委員會審定書	i
誌謝.....	ii
中文摘要.....	iii
Abstract.....	iv
Chapter 1 Introduction.....	1
Reference	4
Chapter 2 Theoretical Background.....	7
2.1 ZrS ₃	7
2.2 SnS ₂	8
2.3 Raman scattering	9
Reference	11
Chapter 3 Experimental Details	13
3.1 Thermal Evaporation System	13
3.2 Chemical Vapour Transport (CVT)	14
3.3 I-V curve Measurement.....	16
3.4 Atomic Force Microscopy (AFM).....	17
3.5 Device Fabrication	18
Chapter 4 Results and Discussion	20
Reference	35
Chapter 5 Conclusion	37



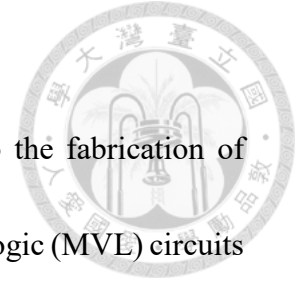
List of figures

Figure 2.1	Schematic representation of ZrS ₃ crystal structure.....	7
Figure 2.2	Schematic representation of SnS ₂ crystal structure.	9
Figure 2.3	Energy-level diagram with Raman scattering excitation.....	10
Figure 3.1	Thermal evaporation system.....	13
Figure 3.2	I-V probe measurement system	16
Figure 3.3	Schematic illustration of the working principle of AFM.....	18
Figure 3.4	Photographic image of AFM.	18
Figure 3.5	Fabrication processes of ZrS ₃ /SnS ₂ heterostructure	19
Figure 4.1	Surface characteristics of ZrS ₃ /SnS ₂ devices.....	27
Figure 4.2	Current–voltage characteristic of ZrS ₃ /SnS ₂ device.....	28
Figure 4.3	Energy band alignment in the ZrS ₃ /SnS ₂ heterojunction.....	29
Figure 4.4	Optical microscopy image of the ZrS ₃ /SnS ₂ heterostructure device	30
Figure 4.5	(a) I_{ds} - V_{ds} characteristic curves of the ZrS ₃ /SnS ₂ device measured at zero gate voltage under illumination of 405 nm wavelength laser at different power intensity. (b) Photocurrent (I_{ph}) estimated from the I_{ds} - V_{ds} curves at $V_{ds} = 5$ V versus laser power intensity. (c) Responsivity (R) and detectivity (D^*) of the ZrS ₃ /SnS ₂ device determined at $V_{ds} = 5$ V plotted as a function of laser power intensity. (d) Photo-switching characteristic of the device under the illumination of laser.	31
Figure 4.6	Photogain plotted as a function of laser power intensity.	32
Figure 4.7	(a-c) Optical microscopy images of the ZrS ₃ device with Ti contact fabricated with different dimension and thickness of ZrS ₃ flakes. (d-f) I_{ds} - V_{ds} characteristic curves of the ZrS ₃ device corresponding to optical images (a), (b), and (c), respectively.	33
Figure 4.8	(a) Optical microscopy image of the ZrS ₃ /SnS ₂ device. (b) I_{ds} - V_{ds}	

characteristic curve of the device at constant gate voltage in the dark condition and the inset represents the corresponding differential conductance plot. (c) $I_{ds}-V_{ds}$ characteristic curve of the device at constant gate voltage in the laser illuminated condition. (d) Differential conductance plotted as a function of applied bias voltage at constant gate voltage in the laser-illuminated condition corresponding to (c).34

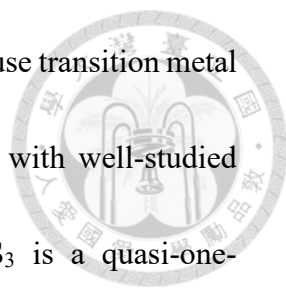


Chapter 1 Introduction



The trend towards compacting electronic gadgets leads to the fabrication of ultra-thin and densely packed electronic circuits. The multi-valued logic (MVL) circuits which have multiple threshold voltages has been a boon to the researchers in this field, which was realized through the non-linear current-voltage behavior in the negative differential resistance (NDR) region in certain devices.¹⁻³ However, the realization of this NDR effect at room temperature has been a major challenge. The incorporation of two-dimensional semiconductor heterostructures has a compelling positive effect in achieving negative differential transconductance and negative differential resistance.⁴⁻⁸ The type-I (straddling gap),⁹ type-II (staggered gap),^{3,10} and type-III (broken gap)^{11,12} band-aligned 2D heterostructures have their own applications. Among these, type-III heterostructure with a broken-gap band alignment has large band offsets resulting in the band-to-band tunneling of carriers from the valence band of one semiconductor to the conduction band of another semiconductor.^{13,14} This interlayer tunneling effect gives rise to the NDR effect in certain heterostructure devices.

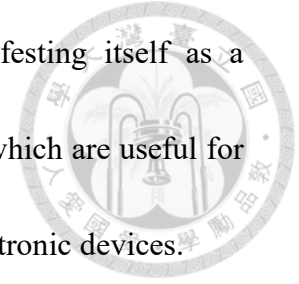
The NDR effect was observed initially in the MoS₂/WSe₂ heterostructure at low temperatures by applying dual gate voltage and by tuning the thickness of the layers.^{10,15} It was also reported in other 2D heterostructures at room temperature such as BP/SnSe₂, BP/ReS₂ and WSe₂/SnSe₂.^{11,12,16,17} However, the stability of black phosphorous (BP)



poses a major challenge in these heterostructures.¹⁸ In this work, we use transition metal trichalcogenides (TMT's) like zirconium trisulphide (ZrS_3) along with well-studied dichalcogenide (SnS_2) to obtain a type-III band alignment. ZrS_3 is a quasi-one-dimensional trichalcogenide semiconductor with a considerable bandgap in the range of ~ 2.1 eV.^{19,20} Recently, there are reports on these ZrS_3 as broadband photodetectors due to their wide band gap and other interesting properties induced by the quantum confinement effect.^{21,22} On the other hand, SnS_2 is a dichalcogenide n-type semiconductor with a bandgap of ~ 2.2 eV.¹⁴

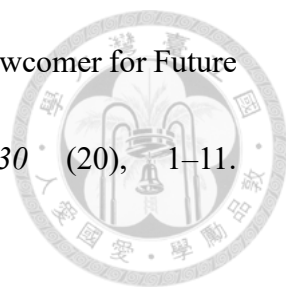
The present work focuses on fabricating a ZrS_3/SnS_2 heterostructure device on SiO_2/Si substrate and carrying out electrical and optical measurements at room temperature to study the NDR effect. The devices were measured in back-gated transistor configuration with 300 nm SiO_2 as a dielectric and observed to exhibit a significant non-linear current-voltage behavior with a considerable peak-to-valley ratio. The influence of band-to-band tunneling at the interface is crucial for the realization of NDR effect which takes place due to the broken gap energy band alignment in the heterostructure. The effect of the metal-induced gap states at the interface between electrode and 2D material in suppressing the NDR effect at room temperature has been elaborated, indicating that in order to observe the NDR effect, the choice of a suitable metal electrode is very important. Due to the wide bandgap of both ZrS_3 and SnS_2 ,

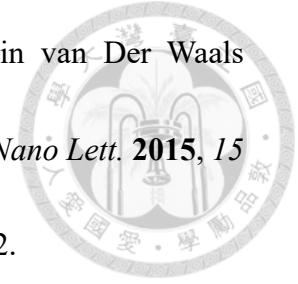
reasonable photoresponsivity was observed in the device manifesting itself as a photodetector. Thus, the present work reports compelling results, which are useful for further study on trichalcogenides and the design of unique optoelectronic devices.



Reference

- (1) Smith. The Prospects for Multivalued Logic: A Technology and Applications View. *IEEE Trans. Comput.* **1981**, 3 (9), 619–634. <https://doi.org/10.1109/TC.1981.1675860>.
- (2) Waho, T, Chen, K.J., Yamamoto, M. Resonant-Tunneling Diode and HEMT Logic Circuits with Multiple Thresholds and Multilevel Output. *IEEE J. Solid-State Circuits* **1998**, 33 (2), 268–274. <https://doi.org/10.1109/4.658629>.
- (3) Paul Inbaraj, C. R.; Mathew, R. J.; Ulaganathan, R. K.; Sankar, R.; Kataria, M.; Lin, H. Y.; Chen, Y. T.; Hofmann, M.; Lee, C. H.; Chen, Y. F. A Bi-Anti-Ambipolar Field Effect Transistor. *ACS Nano* **2021**, 15 (5), 8686–8693. <https://doi.org/10.1021/acsnano.1c00762>.
- (4) Lim, J. H.; Shim, J.; Kang, B. S.; Shin, G.; Kim, H.; Andreev, M.; Jung, K. S.; Kim, K. H.; Choi, J. W.; Lee, Y.; Park, J. H. Double Negative Differential Transconductance Characteristic: From Device to Circuit Application toward Quaternary Inverter. *Adv. Funct. Mater.* **2019**, 29 (48), 1–8. <https://doi.org/10.1002/adfm.201905540>.
- (5) Li, Y.; Wang, Y.; Huang, L.; Wang, X.; Li, X.; Deng, H. X.; Wei, Z.; Li, J. Anti-Ambipolar Field-Effect Transistors Based on Few-Layer 2D Transition Metal Dichalcogenides. *ACS Appl. Mater. Interfaces* **2016**, 8 (24), 15574–15581. <https://doi.org/10.1021/acсами.6b02513>.

- 
- (6) Wakayama, Y.; Hayakawa, R. Antiambipolar Transistor: A Newcomer for Future Flexible Electronics. *Adv. Funct. Mater.* **2020**, *30* (20), 1–11. <https://doi.org/10.1002/adfm.201903724>.
- (7) Li, T.; Li, X.; Tian, M.; Hu, Q.; Wang, X.; Li, S.; Wu, Y. Negative Transconductance and Negative Differential Resistance in Asymmetric Narrow Bandgap 2D-3D Heterostructures. *Nanoscale* **2019**, *11* (11), 4701–4706. <https://doi.org/10.1039/c8nr09674k>.
- (8) Andreev, M.; Choi, J. W.; Koo, J.; Kim, H.; Jung, S.; Kim, K. H.; Park, J. H. Negative Differential Transconductance Device with a Stepped Gate Dielectric for Multi-Valued Logic Circuits. *Nanoscale Horizons* **2020**, *5* (10), 1378–1385. <https://doi.org/10.1039/d0nh00163e>.
- (9) Bellus, M. Z.; Li, M.; Lane, S. D.; Ceballos, F.; Cui, Q.; Zeng, X. C.; Zhao, H. Type-I van Der Waals Heterostructure Formed by MoS₂ and ReS₂ Monolayers. *Nanoscale Horizons* **2017**, *2* (1), 31–36. <https://doi.org/10.1039/c6nh00144k>.
- (10) Roy, T.; Tosun, M.; Cao, X.; Fang, H.; Lien, D. H.; Zhao, P.; Chen, Y. Z.; Chueh, Y. L.; Guo, J.; Javey, A. Dual-Gated MoS₂/WSe₂ van Der Waals Tunnel Diodes and Transistors. *ACS Nano* **2015**, *9* (2), 2071–2079. <https://doi.org/10.1021/nn507278b>.
- (11) Yan, R.; Fathipour, S.; Han, Y.; Song, B.; Xiao, S.; Li, M.; Ma, N.; Protasenko,



- V.; Muller, D. A.; Jena, D.; Xing, H. G. Esaki Diodes in van Der Waals Heterojunctions with Broken-Gap Energy Band Alignment. *Nano Lett.* **2015**, *15* (9), 5791–5798. <https://doi.org/10.1021/acs.nanolett.5b01792>.
- (12) Shim, J.; Oh, S.; Kang, D. H.; Jo, S. H.; Ali, M. H.; Choi, W. Y.; Heo, K.; Jeon, J.; Lee, S.; Kim, M.; Song, Y. J.; Park, J. H. Phosphorene/Rhenium Disulfide Heterojunction-Based Negative Differential Resistance Device for Multi-Valued Logic. *Nat. Commun.* **2016**, *7*, 1–8. <https://doi.org/10.1038/ncomms13413>.
- (13) Kim, S.; Du, H.; Kim, T.; Shin, S.; Song, H. kyo; Kim, H.; Kang, D.; Lee, C. W.; Seo, S. Gate-Switchable Rectification in Isotype van Der Waals Heterostructure of Multilayer $\text{MoTe}_2/\text{SnS}_2$ with Large Band Offsets. *npj 2D Mater. Appl.* **2020**, *4* (1), 1–7. <https://doi.org/10.1038/s41699-020-0149-8>.
- (14) Zhou, X.; Hu, X.; Zhou, S.; Song, H.; Zhang, Q.; Pi, L.; Li, L.; Li, H.; Lü, J.; Zhai, T. Tunneling Diode Based on $\text{WSe}_2/\text{SnS}_2$ Heterostructure Incorporating High Detectivity and Responsivity. *Adv. Mater.* **2018**, *30* (7), 1–8. <https://doi.org/10.1002/adma.201703286>.

Chapter 2 Theoretical Background



2.1 ZrS₃

ZrS₃ is a kind of two-dimensional transition metal trichalcogenides (TMTs) in the type of MX₃ with M a transition metal atom (Zr, Ti... etc.) and X (S, Se... etc.) a chalcogen atom. TMTs have some properties in common. For example: They possess low cleavage energy, so it is easy to exfoliate. Second, the quasi-1D chain-like structure of MX₃ molecules leads to distinctive physical properties. Moreover, the optical band gap of MX₃ materials spans from the visible to the infrared region, making them suitable for a wide range of optoelectronic applications.¹ **Figure 2.1** shows the crystal structure of ZrS₃. The trichalcogenide ZrS₃ single crystals has layered structure crystalized in monoclinic phase. ZrS₃ has a wide direct band gap of 2.13 eV and an indirect band gap of 1.83 eV as a monolayer, offering the potential for effective absorption of visible light.²

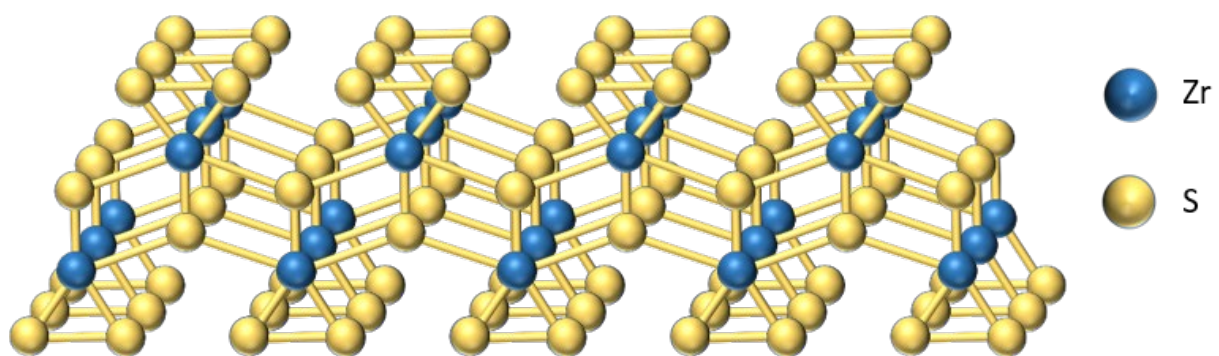
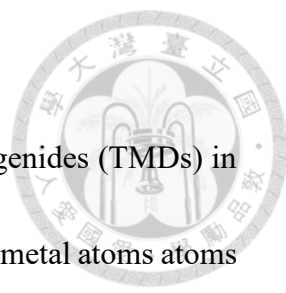
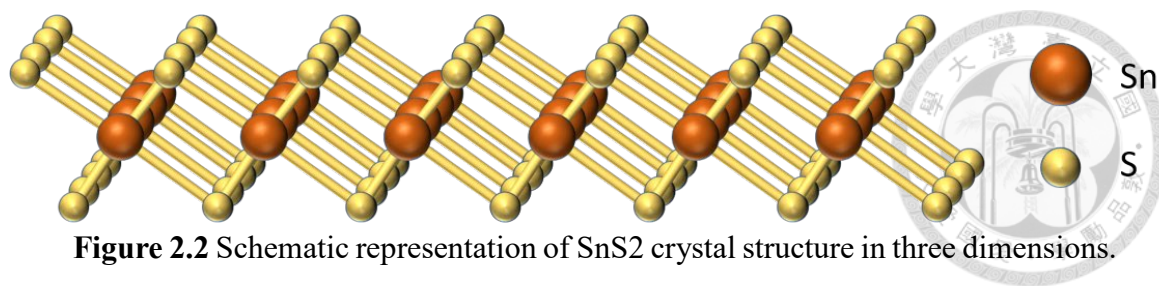


Figure 2.1 Schematic representation of ZrS₃ crystal structure in three dimensions.

2.2 SnS₂



SnS₂ is a kind of two-dimensional transition metal dichalcogenides (TMDs) in the type of MX₂. Monolayer TMDs consist of a layer of M transition metal atoms sandwiched between two layers of X chalcogen atoms. **Figure 2.2** shows the crystal structure of SnS₂. The monolayer SnS₂ has hexagonal lattice and Sn atoms located in the octahedral sites are sandwiched by S atom layers. SnS₂ has attracted considerable interest because of its outstanding electronic, photonic, and optoelectronic properties. These properties encompass high theoretical carrier mobility, stability at the single-layer level, adjustable bandgaps, and a substantial specific surface area, all stemming from its unique ultrathin 2D structures.^{3,4} SnS₂ is considered a promising material for short-channel FETs and integrated logic circuits, owing to its indirect bandgap of around 2.2 eV.⁵ Additionally, its cost-effectiveness, abundance in nature, non-toxic nature, and environmentally friendly attributes make it a more suitable candidate for meeting the demands of next-generation electronics and optoelectronics in comparison to other 2D TMDs.⁶ Furthermore, its flexibility and transparency render it a promising optoelectronic material, particularly for use in wearable electronics applications.⁷



2.3 Raman scattering

Raman spectroscopy, a highly effective experimental technique for identifying material properties, is employed to study the vibrational modes, rotational modes, and other low-frequency modes of lattices and molecules in a system. When a monochromatic laser interacts with sample molecules, light undergoes scattering. If there is an energy exchange between photons and molecules upon inelastic collision, the photons transfer or gain some energy from the sample molecules, resulting in a change in the frequency of light. This phenomenon is known as Raman scattering, and the shift in signal position on the spectrum is referred to as the Raman shift.⁸ The Raman shift does not change with incident laser wavelength, making it possible to understand molecular bonding and structure, furthermore, the properties of a material.

When a sample molecule absorbs an incident photon, it undergoes excitation from its ground state to a virtual energy state. Subsequently, the excited molecule emits a photon and returns to a rotational or vibrational state that differs from the ground state. The energy difference between the ground state and the new state results in the emitted photon having a frequency different from the wavelength of the excitation light. Several

Raman scattering cases are shown in **Figure 2.3**. If the energy of the photon after scattering is lower than that of the incident photon, it is referred to as “Stokes Raman scattering”. If the energy of the photon after scattering is higher, referred to as “Anti-Stokes Raman scattering”.

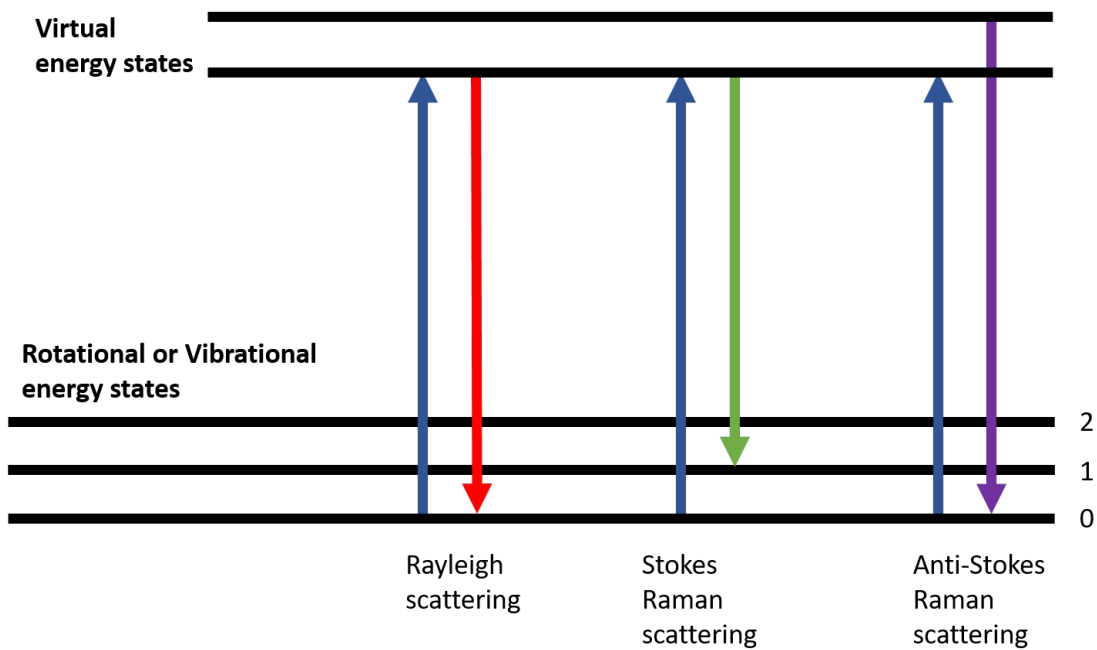
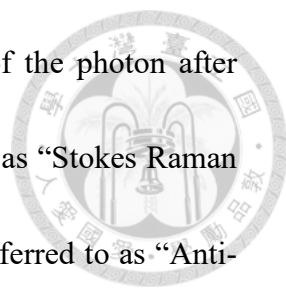
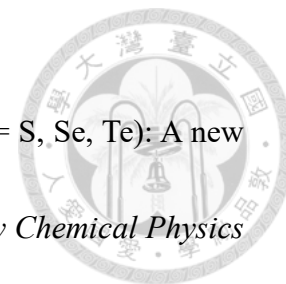


Figure 2.3 Energy-level diagram with Raman scattering excitation.

Reference

- (1) Jin, Y.; Li, X.; Yang, J. Single layer of MX₃ (M= Ti, Zr; X= S, Se, Te): A new platform for nano-electronics and optics. *Physical Chemistry Chemical Physics* **2015**, *17* (28), 18665-18669. <https://doi.org/10.1039/C5CP02813B>
- (2) Drozdowska, K.; Rehman, A.; Rumyantsev, S.; Wurch, M.; Bartels, L.; Balandin, A.; Cywiński, G. Study of ZrS₃-based field-effect transistors toward the understanding of the mechanisms of light-enhanced gas sensing by transition metal trichalcogenides. *Materials Today Communications* **2023**, *34*, 105379. <https://doi.org/10.1016/j.mtcomm.2023.105379>
- (3) Wang, Q. H.; Kalantar-Zadeh, K.; Kis, A.; Coleman, J. N.; Strano, M. S. Electronics and optoelectronics of two-dimensional transition metal dichalcogenides. *Nature nanotechnology* **2012**, *7* (11), 699-712. <https://doi.org/10.1038/nnano.2012.193>
- (4) Butler, S. Z.; Hollen, S. M.; Cao, L.; Cui, Y.; Gupta, J. A.; Gutiérrez, H. R.; Goldberger, J. E. Progress, challenges, and opportunities in two-dimensional materials beyond graphene. *ACS nano* **2013**, *7* (4), 2898-2926. <https://doi.org/10.1021/nm400280c>
- (5) Fan, C.; Li, Y.; Lu, F.; Deng, H. X.; Wei, Z.; Li, J. Wavelength dependent UV-Vis photodetectors from SnS₂ flakes. *RSC advances* **2016**, *6* (1), 422-427.



<https://doi.org/10.1039/C5RA24905H>

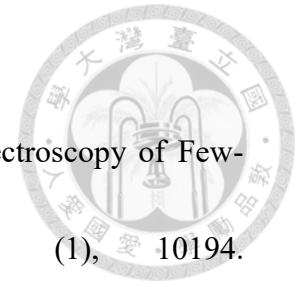
- (6) Sriv, T.; Kim, K.; Cheong, H. Low-Frequency Raman Spectroscopy of Few-Layer 2H-SnS₂. *Scientific reports* **2018**, *8* (1), 10194.

<https://doi.org/10.1038/s41598-018-28569-6>

- (7) Fu, Y.; Gou, G.; Wang, X.; Chen, Y.; Wan, Q.; Sun, J.; Dai, G. High-performance photodetectors based on CVD-grown high-quality SnS₂ nanosheets. *Applied Physics A* **2017**, *123*, 1-8.

- (8) Queisser, H. J. Nonexponential relaxation of conductance near semiconductor interfaces. *Physical review letters* **1985**, *54* (3), 234.

<https://doi.org/10.1103/PhysRevLett.54.234>



Chapter 3 Experimental details

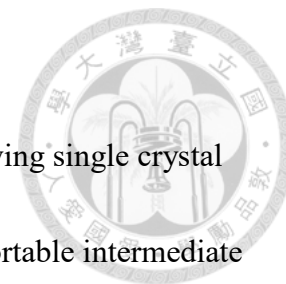
3.1 Thermal Evaporation System

Thermal evaporation is a commonly used thin-film deposition technique for fabricating films on solid substrates. It is a physical vapor deposition (PVD) technique that involves heating the source material to its evaporation point and condensing it onto the substrate surface. The specific steps of thermal evaporation are as follows: Firstly, the source materials titanium and gold are placed on two tungsten boats. Under a vacuum environment (below 2.0×10^{-6} Torr), it is heated by an electrical power source within a chamber. When the temperature reaches the melting point, the source material undergoes a solid-to-gas transition and begins to evaporate. Next, the gaseous material is transported within the evaporation chamber and ultimately condenses onto the surface of the sample (deposited Ti/Au 7 nm/70 nm). **Figure 3.1** shows the setup of thermal evaporation system.



Figure 3.1 Picture of thermal evaporation system.

3.2 Chemical vapour transport (CVT)

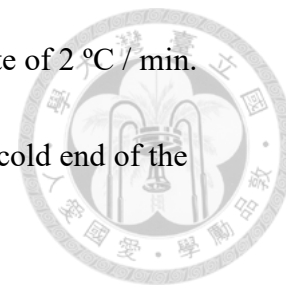


Chemical Vapor Transport (CVT) is a method used for growing single crystal materials. It involves the conversion of precursor gases into transportable intermediate compounds through chemical reactions at high temperatures. These intermediate compounds are then deposited at specific locations by controlling the temperature gradient, resulting in the formation of single crystals.

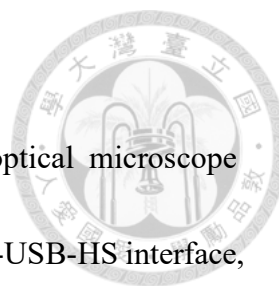
ZrS₃ single crystals were grown using chemical vapor transport (CVT) method with iodine as the transport agent. Initially, ZrS₃ polycrystalline powders were prepared through the solid-state synthesis process. The stoichiometric quantity of high-purity Zr slug (99.99%) and sulphur powder (99.99%) were taken into the silica ampule and sealed at a high vacuum condition to avoid the oxidation of the samples. The mixed compounds were heated at 400 °C and 600 °C for 24 hours, followed by intermediate grinding inside the Argon-filled glove box. During the crystal growth process, the synthesized polycrystalline powders were combined with 200 mg of iodine (I₂) and sealed inside a 40 cm quartz ampule under an internal pressure of approximately 10⁻³ Torr. The sealed quartz ampule was placed inside a horizontal two-zone furnace. The charge end and growth end of the ampule were situated in the hot and cold zones of the furnace, respectively, maintaining a constant temperature of 680 and 620 °C for 200 hours. Once the growth process was completed, the temperature of

the furnace was gradually cooled down to room temperature at a rate of 2 °C / min.

The high-quality ZrS₃ single crystals were then harvested from the cold end of the ampule.



High-quality single crystals of SnS₂ were grown using the chemical vapor transport (CVT) method with iodine as the transport agent. Initially, SnS₂ polycrystalline powders were prepared through the solid-state synthesis process. The stoichiometric quantity of high-purity Sn slug (99.999%) and sulphur powder (99.999%) were taken into the carbon coated silica ampule and sealed at a high vacuum condition. The mixed compounds were heated at 400 °C and 700 °C for 24 hours, followed by intermediate grinding inside the Argon-filled glove box. The synthesized polycrystalline powders were combined with 200 mg of iodine (I₂) and sealed inside a 40 cm quartz ampule under an internal pressure of approximately 10⁻³ Torr. The sealed quartz ampule was placed inside a horizontal two-zone furnace. The charge end and growth end of the ampule were situated in the hot and cold zones of the furnace, respectively, maintaining a constant temperature of 800 and 750 °C for 1 week. Once the growth process was completed, the temperature of the furnace was gradually cooled down to room temperature at a rate of 2 °C / min. The high-quality SnS₂ single crystals were then harvested from the cold end of the ampule.



3.3 I-V Curve Measurement

The measurement of I-V curves is performed using an optical microscope system, three tungsten probes, a Keithley 2400 electrometer, a GPIB-USB-HS interface, and a computer. The $\text{ZrS}_3/\text{SnS}_2$ device is placed on a flat glass slide on the microscope stage. Three tungsten probes make contact with two adjacent Ti/Au electrodes and the back gate, respectively. After ensuring perfect contact of the three probes, the Keithley 2400 is controlled by a computer program to apply bias to the $\text{ZrS}_3/\text{SnS}_2$ device and measure the current. Simultaneously, the computer program records the I-V relation. In addition, we used the Agilent 4156C semiconductor parameter analyzer for $I_{\text{ds}}-V_{\text{g}}$ curve measurement. The wavelength of the laser used for photodetector study is 405 nm.

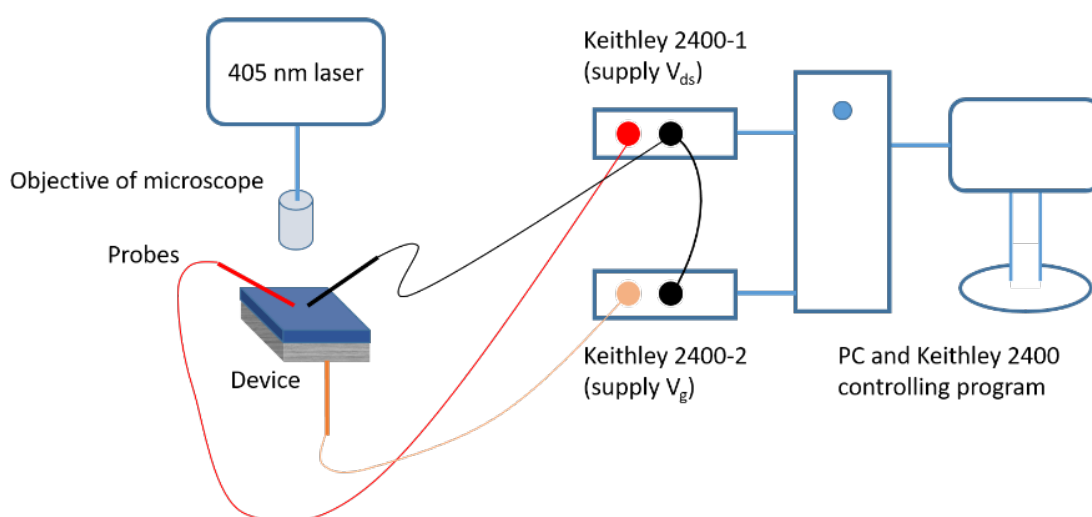
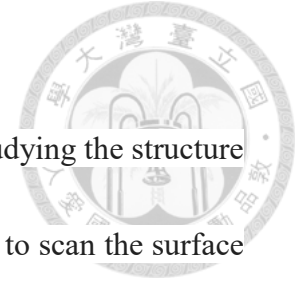


Figure 3.2 Illustration of the I-V probe measurement system.

3.4 Atomic Force Microscopy (AFM)



AFM is a scanning probe microscopy technique used for studying the structure and properties of material surfaces. It employs a non-contact probe to scan the surface of a sample and measures the interaction forces between the probe and the sample to obtain high-resolution images and characterization data.

The working principle of AFM involves suspending the probe above the sample surface and scanning it by controlling the interaction forces between the probe and the sample. The probe typically has a nanoscale tip, and the displacement of the probe is detected using a laser beam or a piezoelectric sensor. The feedback is adjusted based on the interaction forces between the probe and the sample surface.

AFM offers advantages such as the ability to operate in ambient conditions, versatility across different sample types, and the capability for in situ measurements and force spectroscopy analysis. Hence, AFM is an important tool for investigating and understanding surface structures and properties at the nanoscale. The AFM which we

used is from the company of nanosurf. **Figure 3.4** shows the setup of AFM.

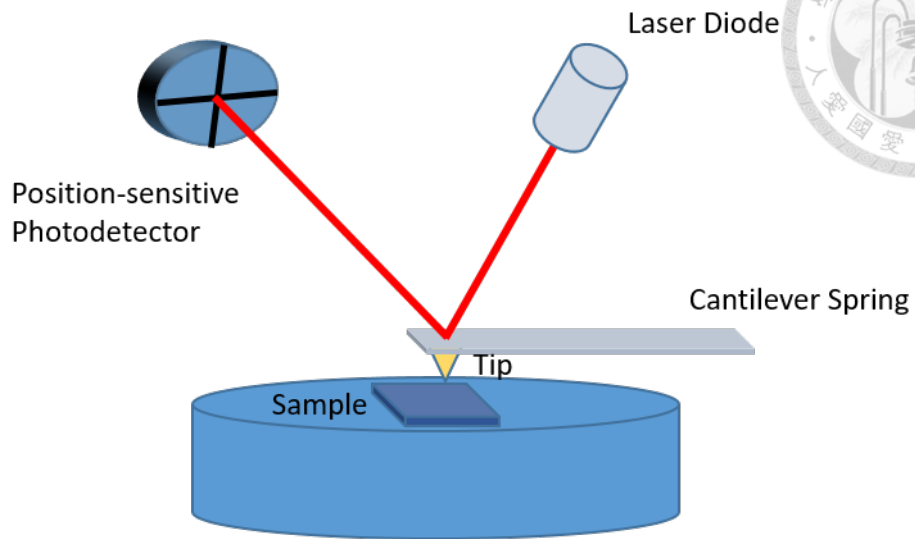


Figure 3.3 Schematic illustration of the working principle of AFM

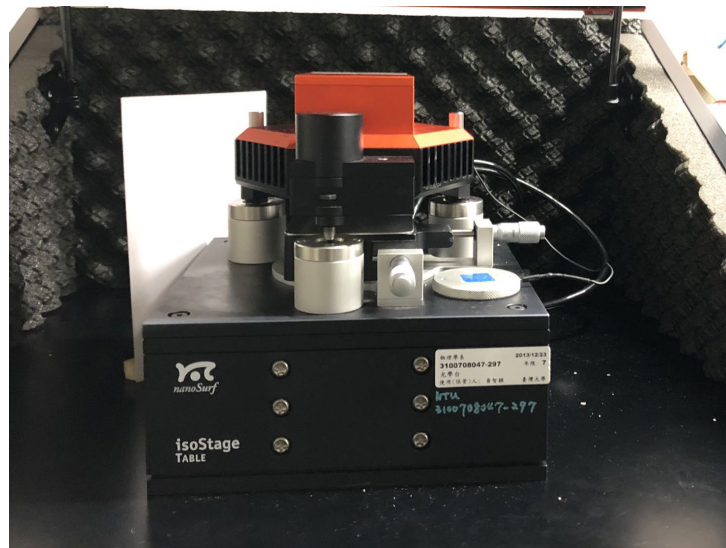


Figure 3.4 Photographic image of AFM

3.5 Device Fabrication

The schematic illustration of each step involved in the $\text{ZrS}_3/\text{SnS}_2$ heterostructure device fabrication is shown in **Figure 3.4**. Initially, SnS_2 flakes were exfoliated and

transferred onto the substrate using a PDMS stamp. After removing the PDMS stamp, the exfoliated ZrS_3 was precisely placed on the SnS_2 flake using the custom-designed micromanipulator. The electrodes were deposited for the assembled heterostructure by fixing a copper mesh using a micromanipulator.

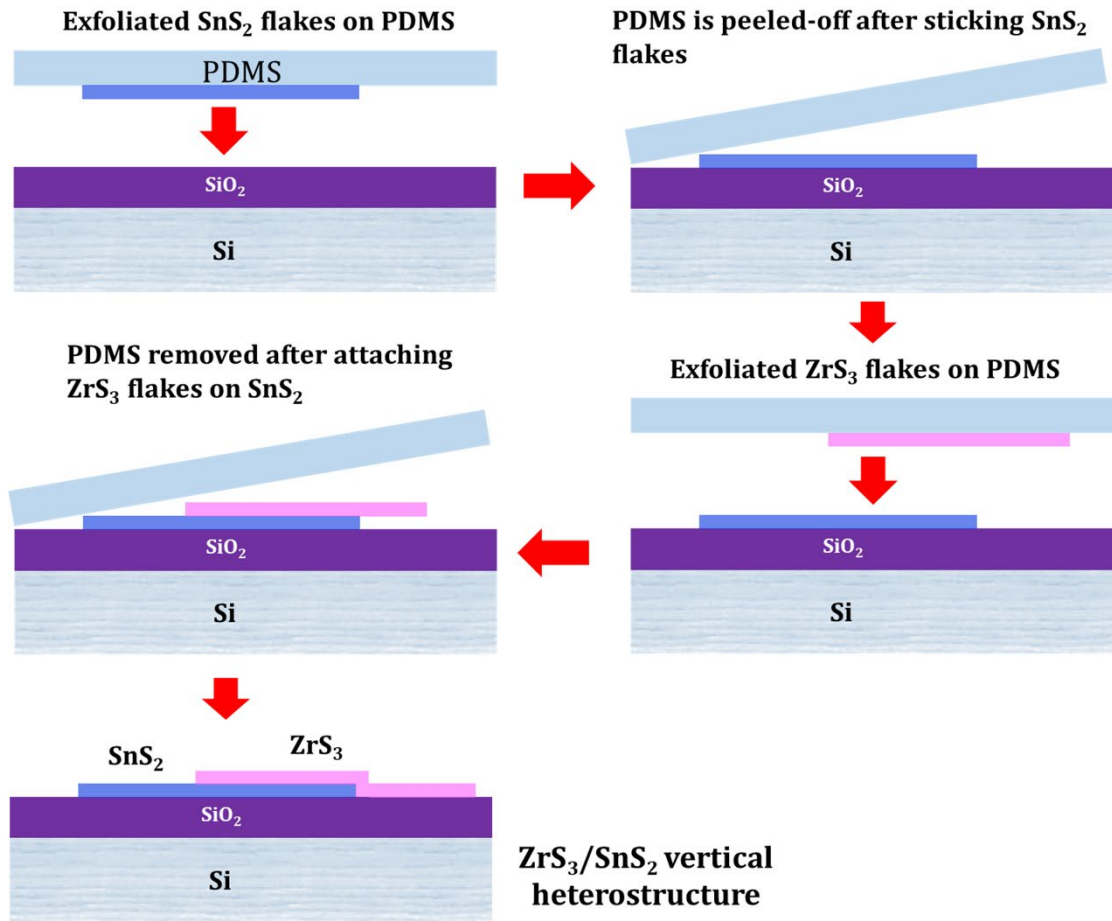
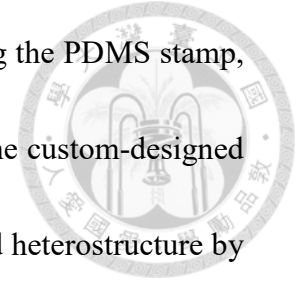
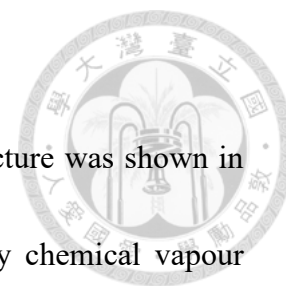


Figure 3.5 Schematic illustration of the step-by-step procedure in the assembly of $\text{ZrS}_3/\text{SnS}_2$ heterostructure.

Chapter 4 Results and Discussion

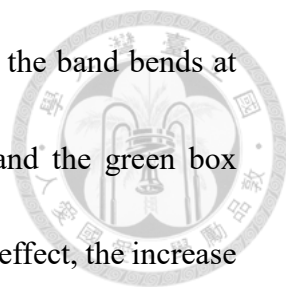


The schematic representation of the $\text{ZrS}_3/\text{SnS}_2$ device structure was shown in **Figure 4.1a**. Both ZrS_3 and SnS_2 single crystals were grown by chemical vapour transport (CVT) technique, which is detailed in the Experimental detail. The as grown trichalcogenide ZrS_3 single crystals has layered structure crystalized in monoclinic phase and are easily exfoliable (**Figure 2.1**).¹ On the other hand, SnS_2 has hexagonal lattice and Sn atoms located in the octahedral sites are sandwiched by S atom layers (**Figure 2.2**).² Dry transfer technique was employed to make the heterostacks and polydimethylsiloxane (PDMS) stamps were used for the transfer process. The schematic depiction of the step-by-step process involved in the heterostructure assembly is represented in **Figure 3.5**. The optical microscopy image of the fabricated $\text{ZrS}_3/\text{SnS}_2$ device was shown in **Figure 4.1b**. Raman spectrum was recorded for the individual layers and the heterojunction region as represented in **Figure 4.1c**. SnS_2 layer exhibits the most prominent out of plane vibration (A_{1g} mode) at 315 cm^{-1} .³ The prominent peaks at 280 cm^{-1} and 320 cm^{-1} in ZrS_3 layers corresponds to A_g^5 and A_g^6 out of plane vibrational modes.⁴ At the $\text{ZrS}_3/\text{SnS}_2$ heterojunction area, the A_{1g} mode of SnS_2 gets superimposed with A_g^6 mode of ZrS_3 indicating a strong interlayer coupling effect. The atomic force microscopy (AFM) scanning over the junction region along with the height profile is shown in **Figure 4.1d**. From the height profile, the thickness of SnS_2

and ZrS₃ layer is estimated to be ~ 15 nm and ~ 19 nm, respectively.

The transfer curves measured for the individual SnS₂ and ZrS₃ devices in the back-gate field effect transistor configuration is represented in **Figure 4.2a**. Both SnS₂ and ZrS₃ layers exhibits n-type nature indicating the majority carriers are electrons. Thus, the junction formed at ZrS₃/SnS₂ is isotype *n-n* heterojunction and the schematic of the device along with circuit connection is shown in **Figure 4.2b**. In the back-gated transistor configuration, the I_{ds} - V_{ds} characteristic curves of the ZrS₃/SnS₂ device was measured at constant gate voltages (V_g) as shown in **Figure 4.2c**. If the curves are observed carefully, a non-linear behavior was observed for gate voltages from 0 to 30 V. The differential conductance (dI_{ds}/dV_{ds}) was calculated from **Figure 4.2c** and plotted against the applied bias as shown in **Figure 4.2d**. The non-linear carrier transport phenomenon is very prominent in the differential conductance indicating a pronounced negative differential resistance (NDR) effect in the device. The inset of **Figure 4.2d** represents the peak-to-valley ratio (PVR) as a function of gate voltage. It can be observed that PVR is higher at zero gate voltage (~ 1.7) and gradually decreases with an increase in gate voltage.

The NDR effect in the device can be understood from the energy band diagram shown in **Figure 4.3**. The energy levels of ZrS₃ and SnS₂ taken from the previous reports are represented in **Figure 4.3a**, which clearly indicates a type-III band alignment



in the heterostructure.⁵ After contact, there is a charge transfer and the band bends at the interface aligning the Fermi level as shown in **Figure 4.3b** and the green box outlined represents a zoomed-in picture at the interface. In the NDR effect, the increase in current is due to the tunneling effect in the broken-gap band alignment and the decreased steady current is due to the diffusion current. At negative bias voltage ($V < 0$ V), the carriers tunnel from the valence band of ZrS₃ to the conduction band of SnS₂ (**Figure 4.3c**). When the positive bias voltage is applied ($0 \text{ V} < V < 1 \text{ V}$), this tunneling of carriers from conduction band of SnS₂ to the valence band of ZrS₃ takes place, which increases the current (**Figure 4.2d**). Till the Fermi level of SnS₂ reaches the valence band of ZrS₃, the tunneling takes place and the current keeps increasing and reaches a peak value. When increasing the applied bias further ($1 \text{ V} < V < 2.4 \text{ V}$), the tunneling effect decreases due to the reduction of the energy states in the bandgap region (**Figure 4.3c**). With further increase in the positive bias ($2.4 \text{ V} < V$), the tunneling effect is greatly reduced and the electrons diffuse through the barrier and there is a steady increase in diffusion current. Thus, the tunneling effect due to the broken-gap band alignment, there is a non-linear increase and decrease in current with increase in applied bias voltage resulting in NDR effect.

Further, photoresponse study has been carried out in the ZrS₃/SnS₂ heterostructure and the optical microscopy image of the device used for this study is

shown in **Figure 4.4**. The I_{ds} - V_{ds} characteristic curve was recorded for the device at zero gate voltage under dark and laser illuminated condition as shown in **Figure 4.5a**. The wavelength of the laser used in this study is 405 nm and the power intensity is tuned using the neutral density filter. The photocurrent ($I_{ph} = I_{light} - I_{dark}$) determined from the I_{ds} - V_{ds} characteristic curve at $V_{ds} = 5$ V is plotted as a function of laser power intensity as shown in **Figure 4.5b**. The generation of photocurrent decreases with decrease in laser power. At the same time, due to the rate of increase in photocurrent per unit power, the photoresponsivity increases with decrease in laser power. The responsivity (R) of the device was estimated by taking the ratio of photocurrent estimated to the power density (P) and device area (A) illuminated by laser.⁶ The equation is written as follows.

$$R = \frac{I_{ph}}{P \times A} \quad (1)$$

The calculated responsivity of the device to the laser illuminated is plotted as a function of laser power intensity in **Figure 4.5c**. The device was able to exhibit a responsivity of 300 mA W⁻¹ for a very low laser power of 4.8 μW cm⁻², which indicates the sensitivity of the device to the photons incident. To establish this quantitatively, the specific detectivity (D*) of the device was determined using the following equation using device area (A), measuring bandwidth (Δf) and noise equivalent power (NEP).⁶

$$D^* = \frac{\sqrt{A \times \Delta f}}{NEP} \quad (2)$$

Here, NEP indicates the minimum optical power that a photodetector can

distinguish from a noise and is dependent on the noise current (I_n). Since the shot noise in the dark current (I_{dark}) influences the noise current in the photodetector, the NEP is estimated using the following equation.^{6,7}

$$\text{Noise current, } I_n = \sqrt{2eI_{\text{dark}}\Delta f} \quad (3)$$

$$NEP = \frac{I_n}{R} = \frac{\sqrt{2eI_{\text{dark}}\Delta f}}{R} \quad (4)$$

$$\text{Therefore, the detectivity can be estimated as, } D^* = \frac{\sqrt{A \times \Delta f}}{NEP} = \frac{R \times \sqrt{A}}{\sqrt{2eI_{\text{dark}}}} \quad (5)$$

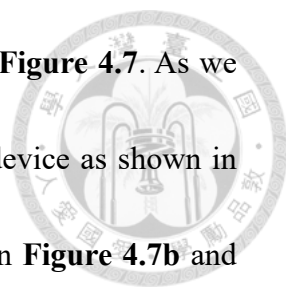
Here, R is the photoresponsivity and e is the electronic charge. The maximum detectivity obtained for our device is 3.6×10^{10} Jones for a laser power of $4.8 \mu\text{W cm}^{-2}$ at $V_{\text{ds}} = 5$ V. The estimated detectivity as a function of laser power is represented in

Figure 4.5c. Another parameter which describes the number of electrons detected per incident photon is photogain (η) which can be estimated as follows.^{6,7}

$$\eta = \frac{R \times h \times c}{e \times \lambda} \quad (6)$$

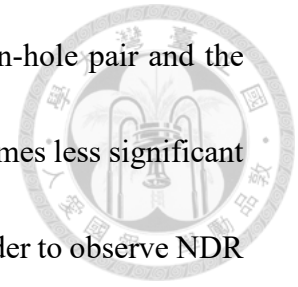
Here, h is the planck's constant, c is the speed of light and λ is the wavelength of the incident laser. The photogain estimated for our device at $V_{\text{ds}} = 5$ V as a function of laser power is represented in **Figure 4.6**. The time-resolved photo-switching stability of the device is shown in **Figure 4.5d**. It can be observed that the current remains stable in the dark condition as well as in the laser-illuminated condition and the change is abrupt with the laser on/off condition.

Furthermore, $I_{\text{ds}}-V_{\text{ds}}$ characteristic curves were measured for ZrS_3 devices with



different structures using only Ti as contact electrode as shown in **Figure 4.7**. As we observe from **Figure 4.7d-f**, the Schottky barrier is weak for the device as shown in **Figure 4.7a**, the device is nearly ohmic for the flake represented in **Figure 4.7b** and **4.7c**. In some thicker devices as in **Figure 4.7a**, where the carrier density is more, the diffusion current is able to overcome the contact resistance and exhibit significant device current. On the other hand, where the dimension and thickness of the flake are very less as in **Figure 4.7c**, the carrier density is less and exhibits a very less device current. The metal-induced gap states at the Ti/ZrS₃ interface plays a vital role in the observation of the NDR effect in the device for they provide the conduction channel of charge carriers and suppress intrinsic conduction properties arising from 2D heterostructure. To emphasize the importance of the contact electrode, the NDR effect observed in another ZrS₃/SnS₂ device with Au/Ti electrode is represented in **Figure 4.8**. In the I_{ds} - V_{ds} characteristic curve in the dark condition (**Figure 4.8b**), the NDR was observed only at higher gate voltages ($V_g = 30$ V and 50 V) and the PVR is very less and the NDR effect is almost absent at $V_g = 0$ and 10 V as observed from the differential conductance represented in the inset of **Figure 4.8b**. On the other hand, under the illumination of a laser, this trend seems to change as can be observed in **Figures 4.8c** and **4.8d**. The NDR effect becomes more pronounced and can be observed obviously starting from $V_g = 0$ to 50 V. This is because under the illumination of laser, the free

charge carrier density is increased due to the separation of electron-hole pair and the effect of Schottky barrier induced by the Fermi level matching becomes less significant resulting in an enhanced NDR effect. This result indicates that in order to observe NDR effect, the choice of a suitable metal electrode is very important.



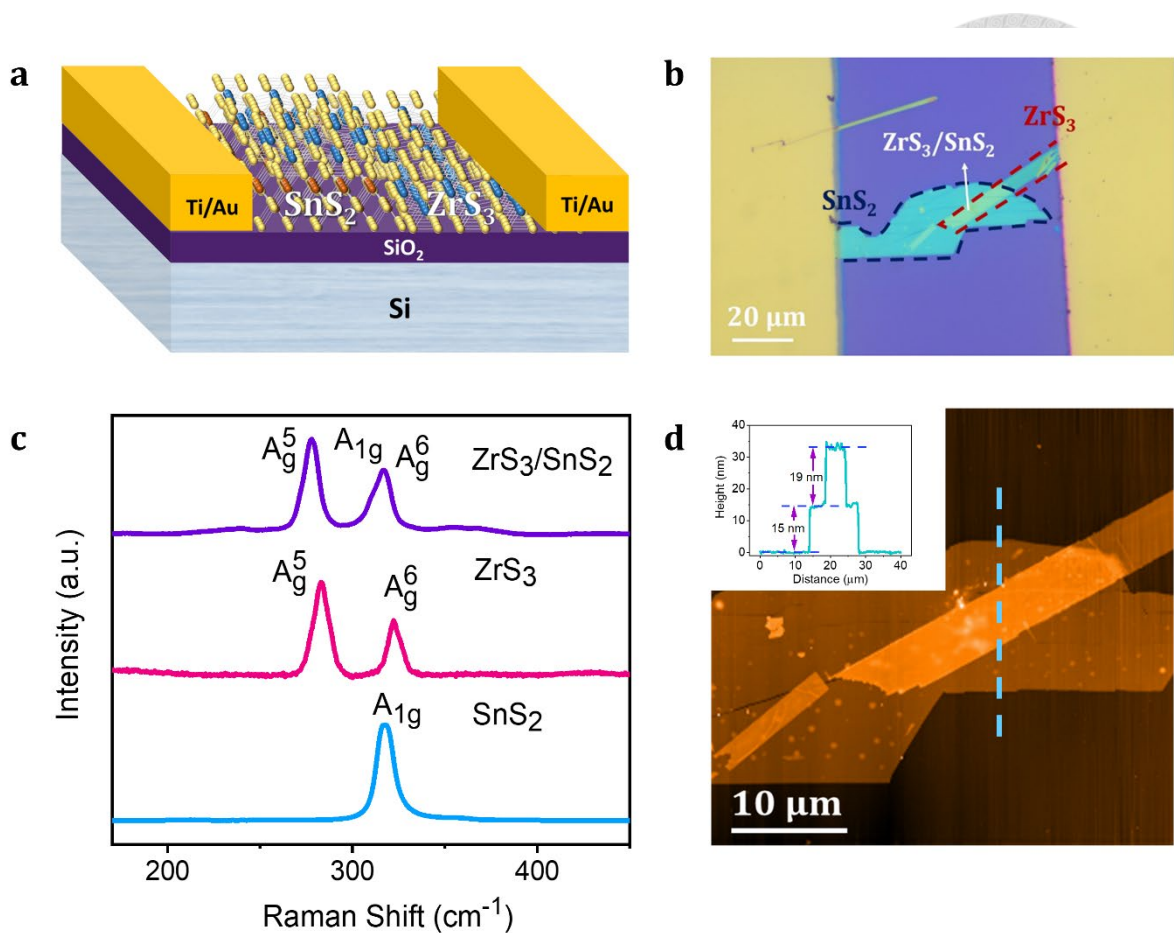


Figure 4.1 (a) Schematic illustration of the ZrS₃/SnS₂ device structure on SiO₂/Si substrate. (b) Optical microscope image of the ZrS₃/SnS₂ heterostack with contact electrodes on SiO₂/Si substrate. (c) Raman spectra of the individual ZrS₃ and SnS₂ layers and the ZrS₃/SnS₂ heterojunction. (d) AFM of the ZrS₃/SnS₂ heterostructure with the inset representing the height profile.

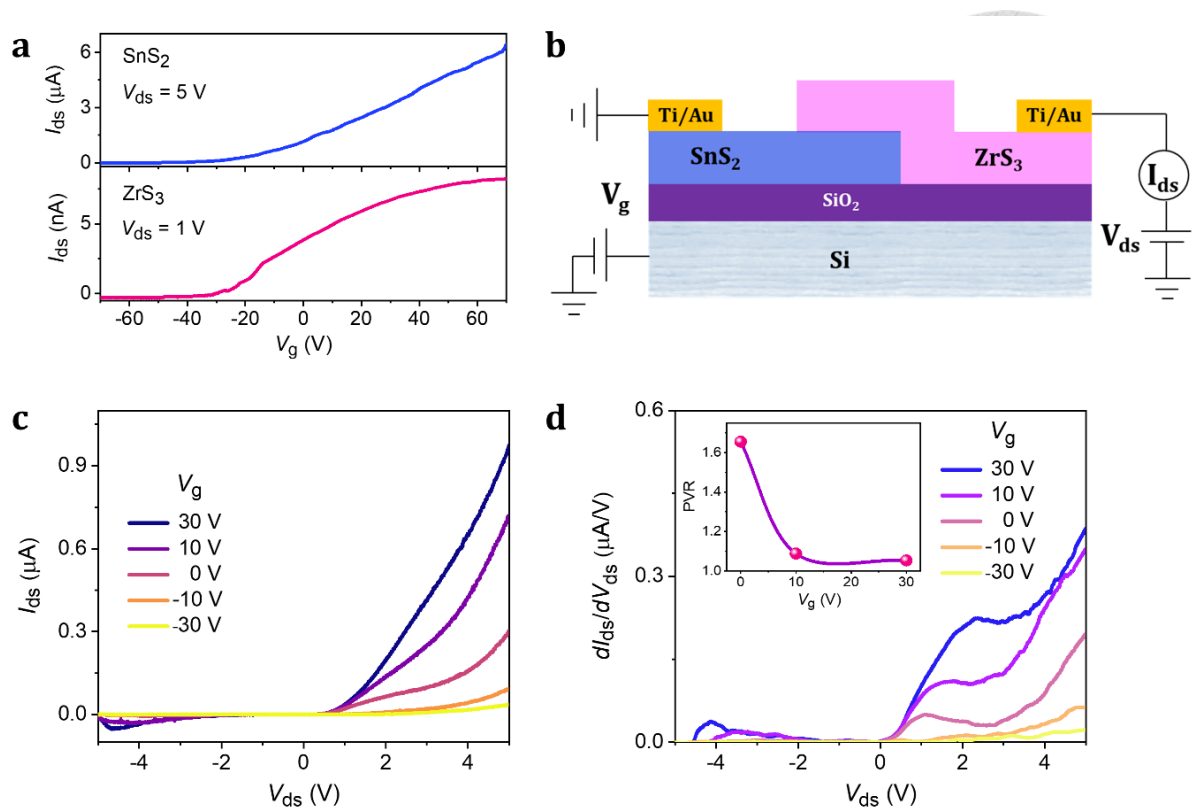


Figure 4.2 (a) Transfer curves of the individual SnS₂ and ZrS₃ device in the back-gated field effect transistor configuration. (b) ZrS₃/SnS₂ device schematic with circuit connection. (c) I_{ds} - V_{ds} characteristic curves of the ZrS₃/SnS₂ device measured at constant gate voltage. (d) Differential conductance (dI_{ds}/dV_{ds}) obtained from the derivative of I_{ds} - V_{ds} curves plotted as a function of applied bias voltage and the inset represents the peak-to-valley ratio (PVR) of the peaks obtained in the differential conductance plotted as a function of applied gate voltage.

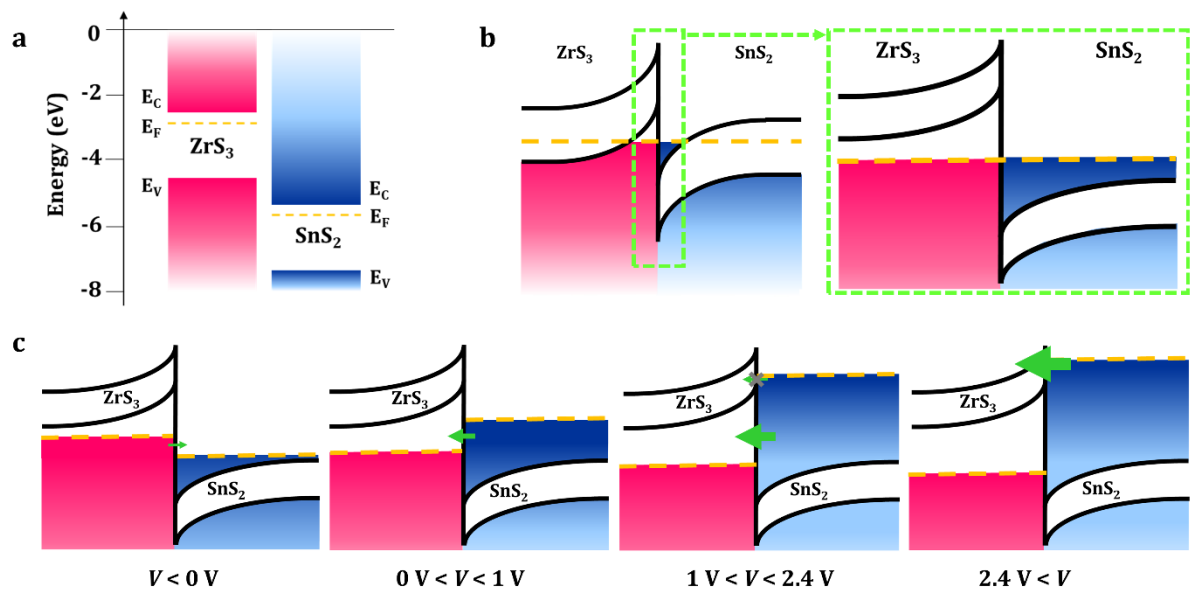


Figure 4.3 (a) Energy levels of the individual ZrS₃ and SnS₂ layers before contact. (b) Energy band alignment in the ZrS₃/SnS₂ heterojunction after contact. (c) Changes in the energy band alignment at different applied bias voltages.

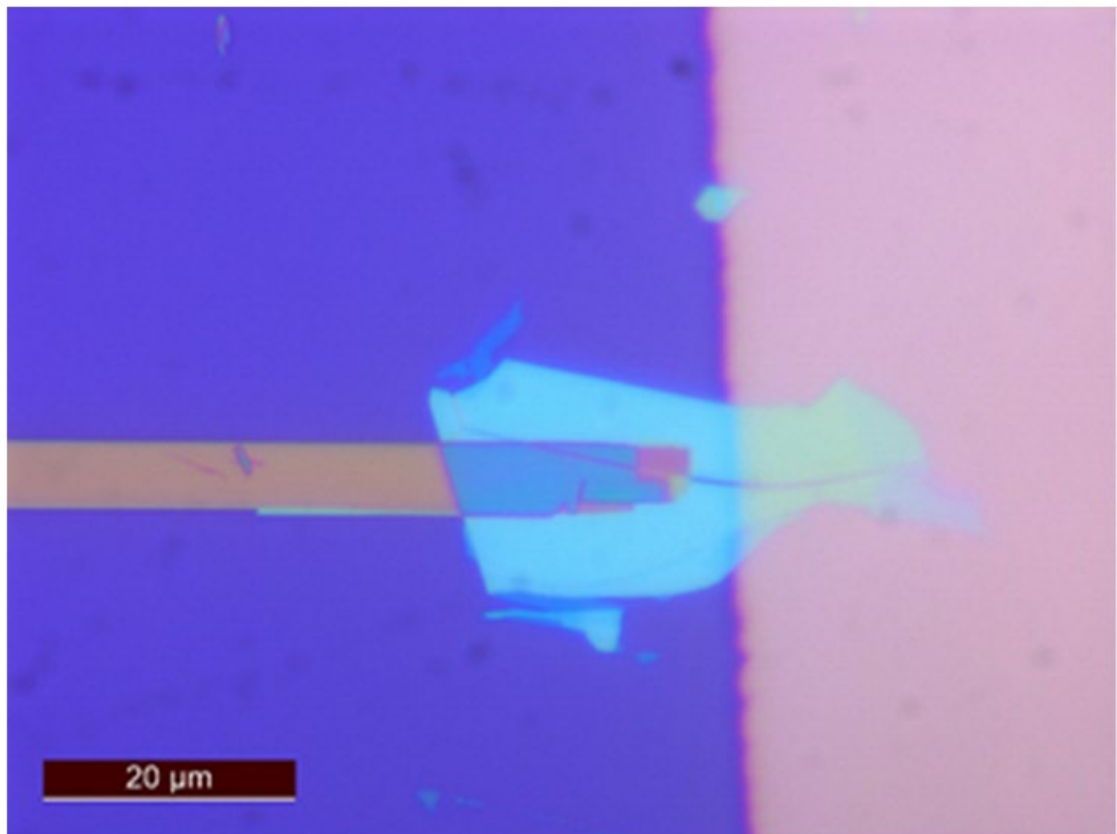


Figure 4.4 Optical microscopy image of the ZrS₃/SnS₂ heterostructure device.

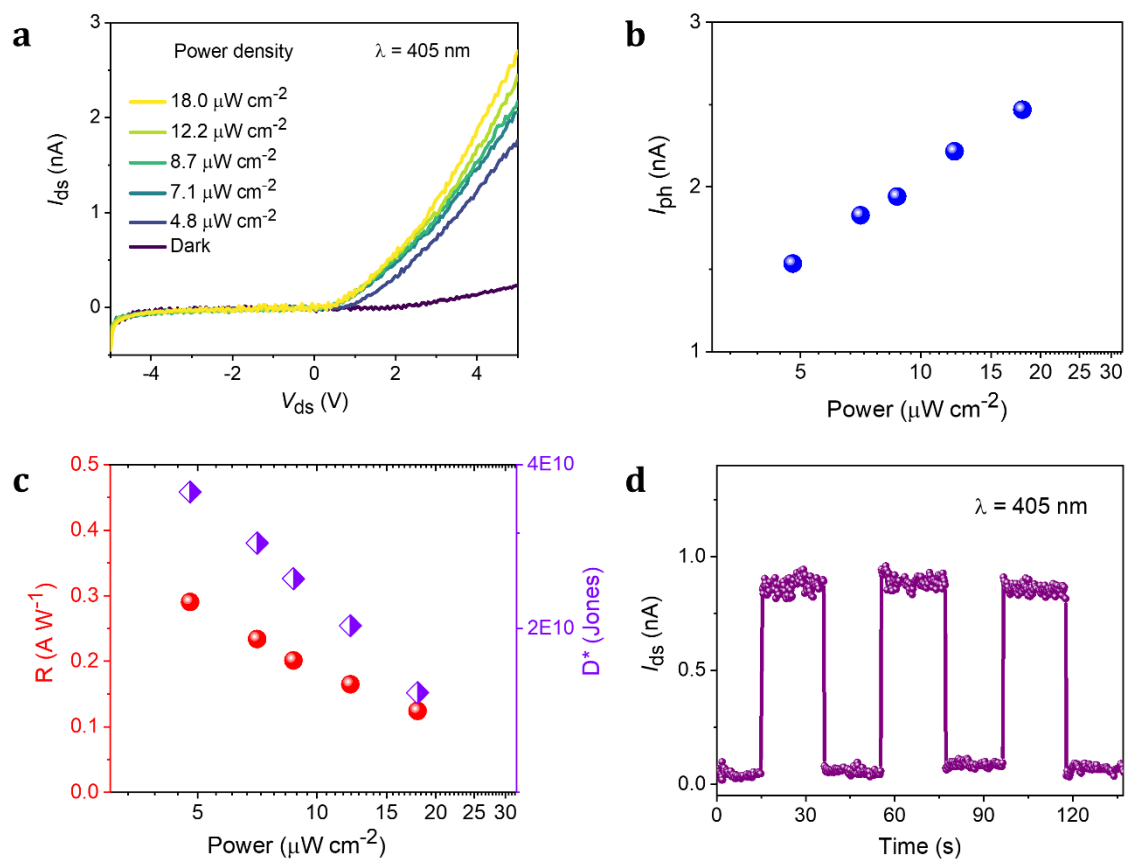


Figure 4.5 (a) I_{ds} - V_{ds} characteristic curves of the ZrS₃/SnS₂ device measured at zero gate voltage under illumination of 405 nm wavelength laser at different power intensity. (b) Photocurrent (I_{ph}) estimated from the I_{ds} - V_{ds} curves at $V_{ds} = 5$ V versus laser power intensity. (c) Responsivity (R) and detectivity (D^*) of the ZrS₃/SnS₂ device determined at $V_{ds} = 5$ V plotted as a function of laser power intensity. (d) Photo-switching characteristic of the device under the illumination of laser.

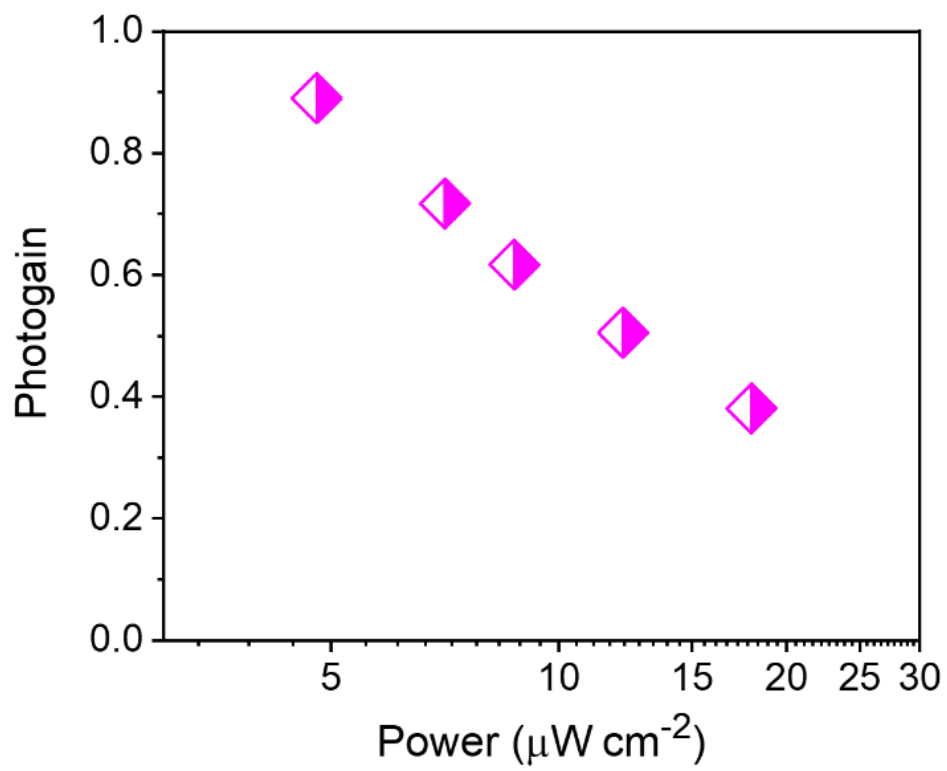


Figure 4.6 Photogain estimated for the $\text{ZrS}_3/\text{SnS}_2$ heterostructure device plotted as a function of laser power intensity.

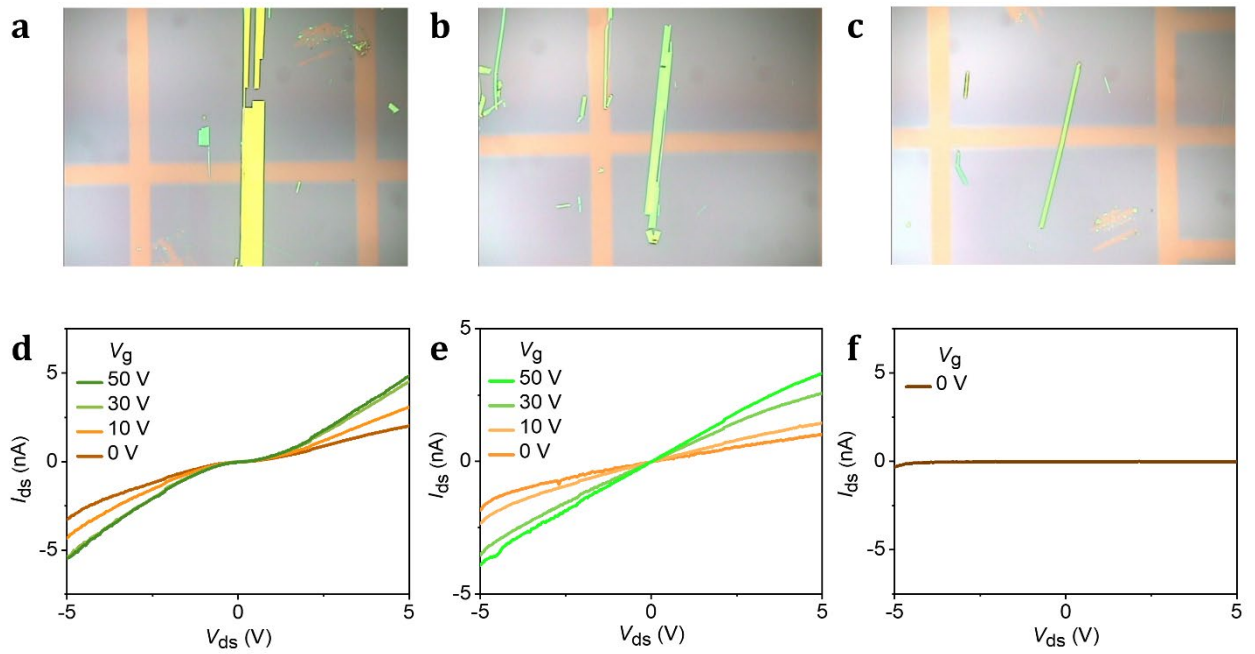


Figure 4.7 (a-c) Optical microscopy images of the ZrS₃ device with Ti contact fabricated with different dimension and thickness of ZrS₃ flakes. (d-f) I_{ds} - V_{ds} characteristic curves of the ZrS₃ device corresponding to optical images (a), (b), and (c), respectively.

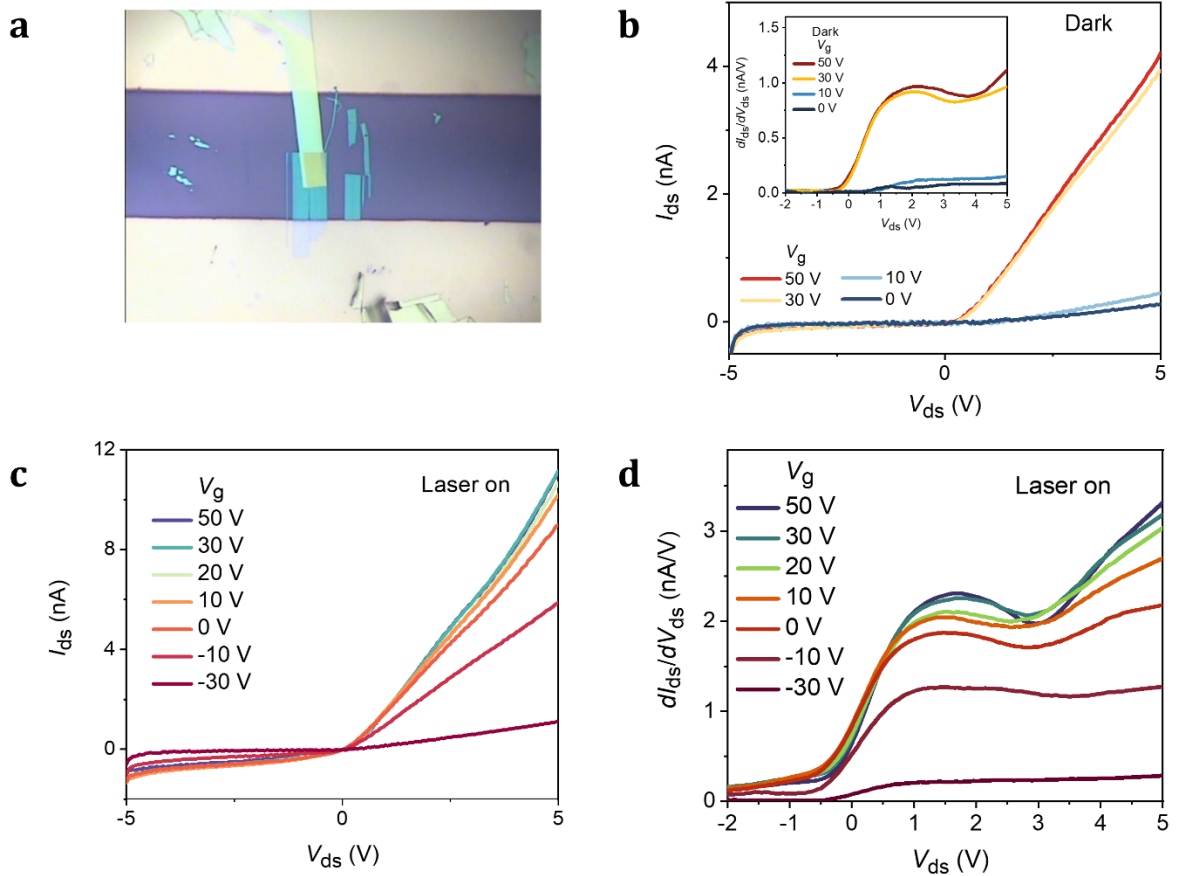
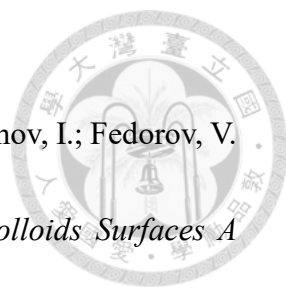
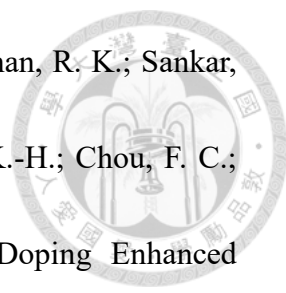


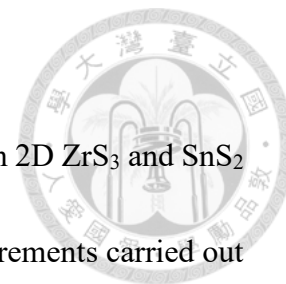
Figure 4.8 (a) Optical microscopy image of the ZrS_3/SnS_2 device. (b) I_{ds} - V_{ds} characteristic curve of the device at constant gate voltage in the dark condition and the inset represents the corresponding differential conductance plot. (c) I_{ds} - V_{ds} characteristic curve of the device at constant gate voltage in the laser illuminated condition. (d) Differential conductance plotted as a function of applied bias voltage at constant gate voltage in the laser-illuminated condition corresponding to (c).

Reference

- 
- (1) Poltarak, P.; Poltarak, A.; Artemkina, S.; Podlipskaya, T.; Asanov, I.; Fedorov, V. ZrS₃: From Crystalline Samples to Colloid Dispersions. *Colloids Surfaces A Physicochem. Eng. Asp.* **2019**, *579* (May), 123667. <https://doi.org/10.1016/j.colsurfa.2019.123667>.
- (2) Li, J.; Shen, J.; Ma, Z.; Wu, K. Thickness-Controlled Electronic Structure and Thermoelectric Performance of Ultrathin SnS₂ Nanosheets. *Sci. Rep.* **2017**, *7* (1), 1–9. <https://doi.org/10.1038/s41598-017-09572-9>.
- (3) Sriv, T.; Kim, K.; Cheong, H. Low-Frequency Raman Spectroscopy of Few-Layer 2H-SnS₂. *Sci. Rep.* **2018**, *8* (1), 2–8. <https://doi.org/10.1038/s41598-018-28569-6>.
- (4) Guo, J.; Tao, J.; Zhang, Z.; Fei, L.; Li, D.; Jadwiszczak, J.; Wang, X.; Guo, Y.; Liao, X.; Zhou, Y. Controllable Thermal Oxidation and Photoluminescence Enhancement in Quasi-1D van Der Waals ZrS₃ Flakes. *ACS Appl. Electron. Mater.* **2020**, *2* (11), 3756–3764. <https://doi.org/10.1021/acsaelm.0c00788>.
- (5) Özçelik, V. O.; Azadani, J. G.; Yang, C.; Koester, S. J.; Low, T. Band Alignment of Two-Dimensional Semiconductors for Designing Heterostructures with Momentum Space Matching. *Phys. Rev. B* **2016**, *94* (3). <https://doi.org/10.1103/PhysRevB.94.035125>.

- 
- (6) Paul Inbaraj, C. R.; Gudelli, V. K.; Mathew, R. J.; Ulaganathan, R. K.; Sankar, R.; Lin, H. Y.; Lin, H.-I.; Liao, Y.-M.; Cheng, H.-Y.; Lin, K.-H.; Chou, F. C.; Chen, Y.-T.; Lee, C.-H.; Guo, G.-Y.; Chen, Y.-F. Sn-Doping Enhanced Ultrahigh Mobility In $1-x$ Sn x Se Phototransistor . *ACS Appl. Mater. Interfaces* **2019**, *11* (27), 24269–24278. <https://doi.org/10.1021/acsami.9b06433>.
- (7) Paul Inbaraj, C. R.; Mathew, R. J.; Haider, G.; Chen, T. P.; Ulaganathan, R. K.; Sankar, R.; Bera, K. P.; Liao, Y. M.; Kataria, M.; Lin, H. I.; Chou, F. C.; Chen, Y. T.; Lee, C. H.; Chen, Y. F. Ultra-High Performance Flexible Piezopotential Gated In $1-x$ Sn x Se Phototransistor. *Nanoscale* **2018**, *10* (39), 18642–18650. <https://doi.org/10.1039/c8nr05234d>.

Chapter 5 Conclusion



In conclusion, a type-III broken gap heterostructure based on 2D ZrS₃ and SnS₂ stacking has been designed and fabricated, and the electrical measurements carried out in the back-gated transistor configuration exhibit a significant NDR effect at room temperature. The tunneling effect due to the broken-gap band alignment was explained based on the energy band diagram. Additionally, the device has been studied as a photodetector due to the significant band gap in both ZrS₃ and SnS₂. The device exhibited a prominent photoresponsivity in the range of 300 mA W⁻¹ for a very low laser power manifesting a strong sensitivity towards the incident photons. The effect of metal electrode caused by the metal-induced gap states in the observation of NDR and the effect of incident light in realizing the NDR effect at room temperature has been discussed in detail. We emphasize here that in order to observe the NDR effect, the choice of a suitable metal electrode is very important. This non-linear carrier transport phenomenon observed at room temperature, which has multiple threshold values can be employed in multi-valued logics and can be a new direction towards the design of future novel optoelectronic devices.